CHINESE OPTICS LETTERS

Vol. 23, No. 4 | April 2025

Compressed sensing reflection matrix optical coherent tomography

Kang Liu (刘 康)[1], Jia Wu (吴 佳)[1], Jing Cao (曹 靖)[2], Rusheng Zhuo (卓儒盛)[1], Kun Li (李 琨)[1], Xiaoxi Chen (陈晓西)[1], Qiang Zhou (周 强)[1,4,5], Pinghe Wang (汪平河)[1*], and Guohua Shi (史国华)[3**]

[1] School of Optoelectronic Science and Engineering, University of Electronic Science and Technology of China, Chengdu 610054, China

[2] Key Laboratory of Biomedical Engineering of Hainan Province, School of Biomedical Engineering, Hainan University, Haikou 570228, China

[3] Suzhou Institute of Biomedical Engineering and Technology, Chinese Academy of Sciences, Suzhou 215163, China

[4] Research Center for Quantum Internet, Tianfu Jiangxi Laboratory, Chengdu 641419, China

[5] Institute of Fundamental and Frontier Sciences, University of Electronic Science and Technology of China, Chengdu 611731, China

*Corresponding author: wphsci@uestc.edu.cn

**Corresponding author: ghshi_lab@126.com

Received September 11, 2024 | Accepted October 21, 2024 | Posted Online April 11, 2025

The reflection matrix optical coherence tomography (RM-OCT) method has made significant progress in extending imaging depth within scattering media. However, the current method of measuring the reflection matrix (RM) through uniform sampling results in relatively long data collection time. This study demonstrates that the RM in scattering media exhibits sparsity. Consequently, a compressed sensing (CS)-based technique for measuring the RM is proposed and applied to RM-OCT images. Experimental results show that this method requires less than 50% of the traditional sampling data to recover target information within scattering media, thereby significantly reducing data acquisition time. These findings not only expand the theory of the RM but also provide a more efficient measurement approach. This advancement opens up broader applications for CS techniques in RM-OCT and holds great potential for improving imaging efficiency in scattering media.

Keywords: reflection matrix; compressed sensing; optical coherence tomography; scattering media.
DOI: 10.3788/COL202523.041102

1. Introduction

In regions of multiple scattering, the direction of photon propagation becomes stochastic, resulting in a loss of imaging capability. Consequently, the majority of optical techniques used for imaging deep within tissues rely on single-scattering photon imaging[1–4]. To overcome the challenges of multiple scattering, optical coherence tomography (OCT) techniques employing coherent gating have been developed to isolate and extract single-scattering photons more effectively[5–9]. Compared to traditional microscopy, OCT significantly enhances imaging depth. However, as the depth increases, the number of single-scattering photons decreases exponentially, limiting its imaging capability to within a few transport mean free paths in scattering tissues[10,11]. The recently introduced Smart-OCT has enhanced the imaging depth of OCT using a reflection matrix (RM)[12]. Current methods for measuring the RM in scattering media involve techniques such as phase-shifting[13–15] or heterodyne detection[16–18]. However, these methods require detectors to measure all sampling points to ensure accuracy and high resolution, which increases the burden of transmission and processing, thereby limiting measurement speed. Furthermore, the theoretical basis for the RM in scattering media assumes that photon propagation in static media is a linear and time-invariant process[19–21]. As the measurement time increases, imaging systems become more susceptible to environmental changes[22]. This is especially true in dynamic environments like blood flow and heartbeat, where the properties of imaging targets or scattering media can change rapidly[17]. This leads to image capture delays and an inability to accurately reflect instantaneous states. In large-scale imaging, the system must balance high resolution with wide coverage while also capturing fine details, such as detecting small lesions in medical imaging. Therefore, reducing RM measurement time is crucial for improving imaging efficiency and accuracy.

Compressed sensing (CS) technology is a powerful tool for image reconstruction. By leveraging the sparsity of signals, it accurately reconstructs data from minimal random sampling, thereby reducing the volume of data required for collection,

transmission, and storage. Initially proposed as a mathematical theory[23,24], CS has been applied to medical imaging fields such as magnetic resonance imaging and photoacoustic imaging[25,26]. Subsequently, CS was introduced into the field of OCT[27] and experimentally validated for image data reconstruction[28]. This includes improvements in CS methods and sparse camera sampling approaches[29,30]. To accelerate the CS reconstruction process, computer systems equipped with graphics processing units (GPUs) have been utilized, enabling real-time, rapid CS reconstruction[31,32].

In this paper, a novel technique is introduced for measuring the RM of scattering media using CS and applied to reflection matrix optical coherence tomography (RM-OCT) imaging. The sparsity of RM in scattering media was first validated through an electric field Monte Carlo model, confirming the feasibility of using CS for measurement. Experimental measurements and imaging of the RM in scattering media were then conducted. By exploiting the RM's sparsity, the matrix can be reconstructed from a subset of sampling points. Results indicate that this method requires less than 50% of the data used in traditional sampling methods to recover imaging target information in scattering media, significantly reducing data acquisition time. This approach has substantial potential to enhance imaging efficiency in scattering media.

2. Methods and Materials

CS is a technique based on the sparsity of signals[23,24]. By utilizing signal sparsity in specific domains, CS can reconstruct the original signal with fewer measurements than the Nyquist limit. In scattering media, multiple scattering leads to highly random photon trajectories, resulting in a relatively small proportion of single scattering components within the RM[12,14,33,34]. However, single-scattering events are closely related to specific light paths and the local structure of the medium. Theoretically, information related to single scattering is primarily concentrated along the diagonal and nearby regions of the RM, while the effects of multiple scattering are represented by the off-diagonal elements[14,18,35,36]. This characteristic suggests that the RM has a sparse structure, providing a theoretical basis for applying CS measurement techniques to the RM.

Figure 1(a) illustrates the schematic of the RM-OCT system. The system uses a laser centered at 790 nm as its light source. A spatial light modulator (SLM) performs biaxial scanning by projecting a set of phase patterns onto the area of interest. Subsequently, a CCD is used to collect backscattered photons from the illuminated area on the imaging plane. The detailed description of the RM-OCT experimental setup is shown in Refs. [16–18].

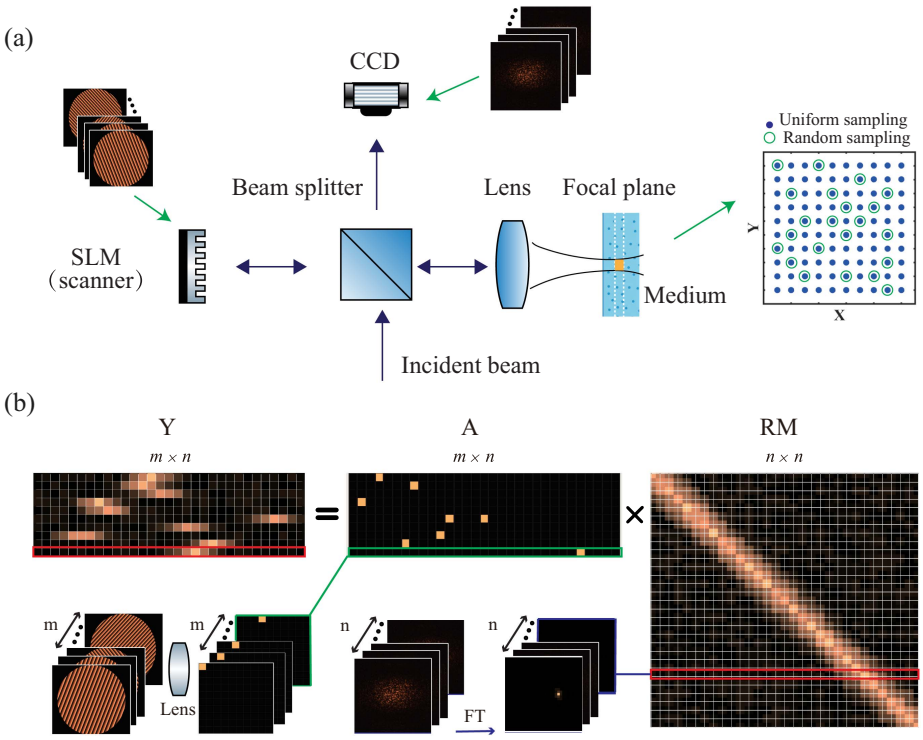

Fig. 1. Schematic and principles of compressed sensing (CS) reflection matrix optical coherence tomography (RM-OCT). (a) Schematic of the RM-OCT system: A laser centered at 790 nm serves as the light source, with a spatial light modulator (SLM) performing biaxial scanning by projecting phase patterns onto the target area. A CCD camera collects backscattered photons. (b) Principle of RM measurement based on CS: where Y is an observation matrix of size $(m \times n)$ with $m < n$, A is a measurement matrix of size $(m \times n)$, and RM is the reflectance matrix of size $(n \times n)$ to be solved.

Figure 1(b) illustrates the principle of RM reconstruction based on CS. The traditional method for constructing an RM first obtains the light field information at each focal point on the imaging location through uniform scanning. Next, the acquired light field information is subjected to a Fourier transform, and finally, it is reordered according to the scanning sequence to generate a two-dimensional reflectance matrix. To reduce sampling time, a reflectance matrix measurement technique is proposed based on CS. A small amount of light field information obtained through random sampling is used to reconstruct the complete reflectance matrix. The measurement process for the reflectance matrix based on CS can be modeled as[37]

$$Y = A \times \mathrm{RM}, \tag{1}$$

where Y is an $(m \times n, m < n)$ observation matrix obtained from sampling, A is an $(m \times n)$ measurement matrix, and RM is an $(n \times n)$ reflectance matrix to be solved.

Based on prior information, the RM primarily reflects the information related to single scattering events along the diagonal and its adjacent regions, while the elements away from the diagonal are mainly associated with multiple scattering effects[35]. The following optimization problem is formulated:

$$\min_{\mathrm{RM}} \| Y - A \times \mathrm{RM} \|_F^2 + \lambda \sum_{i,j} W_{i,j} |\mathrm{RM}_{i,j}|. \tag{2}$$

Here, the first term $\| Y - A \times \mathrm{RM} \|_F^2$ represents the data fidelity term, ensuring the accuracy of the reconstructed RM, while the second term is a position-weighted L_1 regularization term, promoting sparsity in the matrix RM, particularly for elements away from the diagonal. The notation $\| \cdot \|_F$ represents the Frobenius norm. The Frobenius norm is a matrix norm used to measure the square root of the sum of the squares of the matrix elements. The element $\mathrm{RM}_{i,j}$ represents the value at the ith row and jth column of the RM, where $i, j = 1, 2, \ldots, n$. The summation $\sum_{i,j}$ applies to all elements of the matrix, ensuring that the regularization term covers all possible index pairs. The position weights $W_{i,j}$ are designed as

$$W_{i,j} = \exp(\alpha |i - j|), \tag{3}$$

where α is a parameter controlling the rate of decay, ensuring that elements near the diagonal receive less penalization, while elements further from the diagonal are penalized more heavily. This careful weighting helps balance the risk of overfitting by emphasizing the importance of the significant elements close to the diagonal while discouraging the influence of less relevant elements further away, thus enhancing the robustness of the reconstruction.

To address this sparse constraint problem, we employ the alternating direction method of multipliers (ADMM). By introducing an auxiliary variable Z, the optimization problem can be reformulated as [38–40]

$$\min_{\mathrm{RM}, Z} \| Y - A \times \mathrm{RM} \|_F^2 + \lambda \sum_{i,j} W_{i,j} |Z_{i,j}|, \tag{4}$$

$$\text{subject to} \quad Z = \mathrm{RM}. \tag{5}$$

The ADMM-solving process consists of the following steps:

1) Updating RM:

$$\mathrm{RM}^{k+1} = \arg\min_{\mathrm{RM}} \| Y - A \times \mathrm{RM} \|_F^2 + \frac{\rho}{2} \| \mathrm{RM} - Z^k + U^k \|_F^2. \tag{6}$$

This step is a quadratic optimization problem and can be solved using gradient descent methods[41,42].

2) Updating Z:

$$Z^{k+1} = \arg\min_{Z} \lambda \sum_{i,j} W_{i,j} |Z_{i,j}| + \frac{\rho}{2} \| \mathrm{RM}^{k+1} - Z + U^k \|_F^2. \tag{7}$$

This step is solved via the soft-thresholding operation:[43,44]

$$Z_{i,j}^{k+1} = \mathrm{sign}(\mathrm{RM}_{i,j}^{k+1} + U_{i,j}^k) \cdot \max\left(|RM_{i,j}^{k+1} + U_{i,j}^k| - \frac{\lambda W_{i,j}}{\rho}, 0 \right). \tag{8}$$

The soft-thresholding operation encourages sparsity in Z, particularly in elements away from the diagonal.

3) Updating the Lagrange multiplier U:[45,46]

$$U^{k+1} = U^k + (\mathrm{RM}^{k+1} - Z^{k+1}). \tag{9}$$

This step ensures that the constraint $Z = \mathrm{RM}$ is gradually enforced during the iterative process.

The above steps are iterated until convergence.

After reconstructing the RM, it is subjected to singular value decomposition (SVD), as shown in Fig. 2(a). By performing SVD on the RM, the statistical characteristics of the scattering pattern can be obtained. The SVD of the RM can be expressed as[16]

$$\mathrm{RM} = U \Sigma V^* \tag{10}$$

where U and V are the orthogonal matrices, V^* represents the conjugate transpose of matrix V, and Σ is a diagonal matrix consisting of the real positive singular values in decreasing order, $\sigma_1 > \sigma_2 > \ldots > \sigma_n$, where n is the size of Σ. Larger singular values correspond to single-scattering photons, while smaller singular values correspond to multiple-scattering photons. By selecting the appropriate singular vectors for reconstruction[12], it is possible to separately reconstruct images of the single-scattering light field (I_{ss}) and the multiple-scattering light field (I_{ms}), as shown in Fig. 2(b)[12,14],

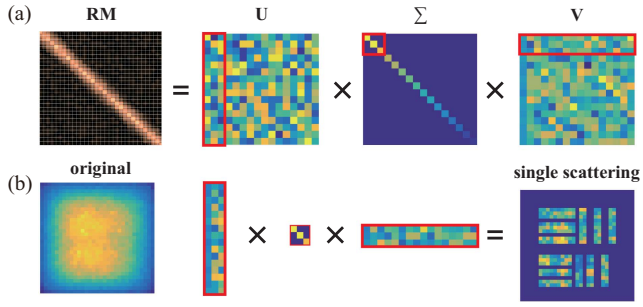

Fig. 2. SVD of the reflection matrix and image reconstruction. (a) SVD: The reflection matrix (RM) is decomposed using singular value decomposition. Larger singular values correspond to single-scattering photons, while smaller values are associated with multiple-scattering photons. (b) Image reconstruction: Images of single scattering (I_{ss}) are reconstructed by applying the Hadamard product to the reshaped singular vectors, utilizing the selected singular values.

$$I_{\mathrm{ss}} = \sum_{i=1}^{t} \sigma_i |\bar{U}_i \circ \bar{V}_i|, \tag{11}$$

$$I_{\mathrm{ms}} = \sum_{i=t}^{n} \sigma_i |\bar{U}_i \circ \bar{V}_i|, \tag{12}$$

where $\bar{U}_i$ and $\bar{V}_i$ are the wavefronts reshaped from the vectors U_i and V_i, respectively, and the reshaping order matches the scanning trajectory of the light field sampling window. The symbol $\circ$ denotes the Hadamard product. t is the threshold for distinguishing between single- and multiple-scattering light fields.

3. Results

To evaluate the feasibility of using CS for RM measurement in complex scattering environments, we first conducted a simulation experiment using the electric field Monte Carlo method, which was developed by Xu and his colleagues[47–49]. Unlike traditional intensity-based Monte Carlo simulations, the electromagnetic compatibility (EMC) method tracks the changes in the electric field during each scattering event, preserving phase information. These changes are analyzed based on Mie scattering theory, allowing for a more comprehensive analysis of the interactions of light within complex media. For simplicity, a "sandwich" structure sample was designed. Under linearly polarized coherent illumination with a central wavelength of $\lambda = 790$ nm, the top layer contains scatterers with absorption characterized by a mean free path $l_t = 1.05$ μm, a refractive index of $n = 1.60 + 0.25i$, an anisotropic factor of $g = 0.210$, and a thickness of $3l_t$. The middle layer contains two different types of scatterers: (1) those identical to the top layer and (2) those with reduced absorption arranged in a USAF target pattern. The scatterers in the USAF target pattern have a mean free path of $l_{t'} = 19.00$ μm, a refractive index of $n' = 1.60 + 0.002i$, an anisotropic factor of $g' = 0.050$, and a thickness of $2l_t$. The bottom layer has the same parameters as the top layer. To compare the effects of different sampling methods on RM measurement, both uniform and random sampling were performed on the sample, as shown in Fig. 3(a). The USAF target in the middle layer is illustrated in Fig. 3(b), and the image obtained under coherent illumination is presented in Fig. 3(c). Figures 3(d) and 3(e), respectively, show the RM obtained from uniform sampling (with 51 × 51 sampling points) and 50% random sampling. The RM was then subjected to SVD, with the singular value distribution displayed in Fig. 3(f). The top 20 singular values were selected for the light field image reconstruction, as shown in Figs. 3(g) and 3(h), which present the reconstructed light field images from uniform and sparse sampling, respectively. Figure 3(i) shows the intensity distribution along the white dashed lines in Figs. 3(g) and 3(h), highlighting the details of the reconstruction quality. To further evaluate the impact of different sampling rates on RM measurement, the mean squared error (MSE)[50], structural similarity index (SSIM)[51], and correlation coefficient (CC)[52] were used for quantitative analysis. The MSE measures the difference between the reconstructed and reference images (uniform sampling), the SSIM evaluates the similarity in brightness, contrast, and structure, and the CC measures the linear correlation between the two images. From the quantitative analysis of Figs. 3(g) and 3(h), the MSE, SSIM, and CC values are 0.0038, 0.9528, and 0.975, respectively, indicating that the RM reconstructed using CS retains consistent information with uniform sampling. This supports the feasibility of using CS for RM measurement in scattering media.

To further validate the effectiveness of CS-based RM measurement in scattering media, experiments were designed and conducted at different sampling rates. In the experiment, a silicone rubber phantom material with a thickness of approximately 2 mm was used, with 10 g of titanium dioxide added to every 100 g of silicone rubber to enhance its scattering characteristics. The light beam was focused at a depth of approximately 0.7 mm within the sample to ensure a more accurate measurement of scattering properties deep within the sample. According to a predefined scanning strategy, both uniform sampling and random sampling were performed on the sample to compare the effects of different sampling methods on RM measurement. Uniform sampling utilized a total of 961 scanning points (31 × 31), covering an area of approximately 70 μm × 70 μm in the region of interest. The acquisition time for each scanning point was 80 ms. Figures 4(a)–4(c) show the RM distributions under 30% and 50% random sampling rates, as well as uniform sampling. Figure 4(d) presents the singular value distribution of the RM under different sampling rates. Although there are some differences in the singular value distribution between lower sampling rates (e.g., 50%) and uniform sampling, the major high singular values remain relatively consistent. This indicates that, even at lower sampling rates, the main features of the signal can still be effectively recovered, as shown by the light field distributions corresponding to the dashed lines in Figs. 4(a) and 4(b). Figure 4(e) illustrates the intensity distribution along the blue dashed lines in Figs. 4(a)–4(c). Figure 4(f)

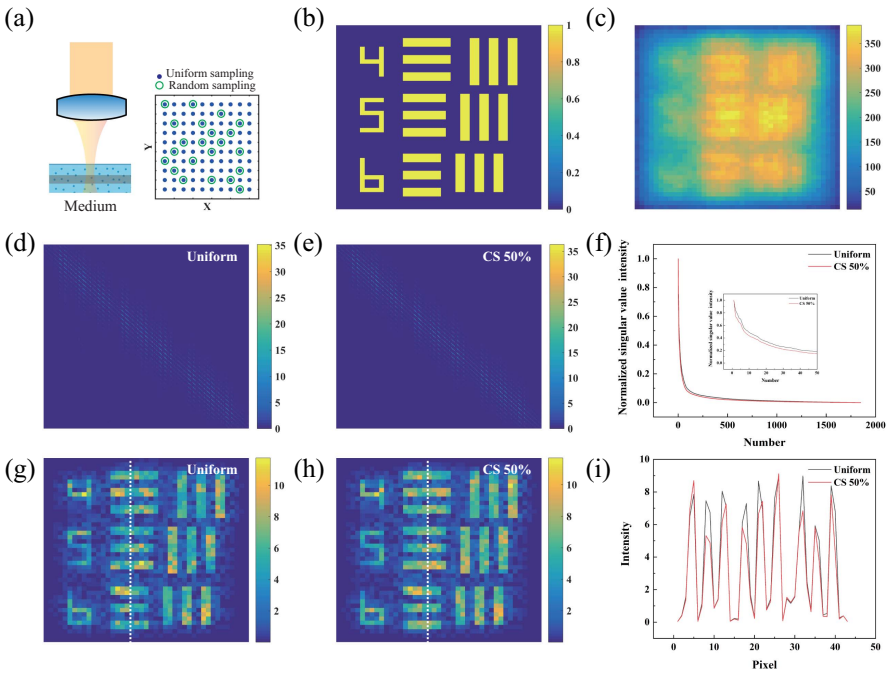

Fig. 3. Electric field Monte Carlo experiments are conducted to evaluate the effectiveness of CS in RM measurements. (a) Simulated "sandwich" structure sample with scattering properties. (b) Hidden USAF target pattern in the middle layer. (c) En face image of the sample under coherent illumination. (d) RM obtained via uniform sampling (51 point × 51 point). (e) RM obtained from 50% random sampling. (f) Singular value distributions for (d) and (e). (g) Image reconstruction from uniform sampling. (h) Image reconstruction from 50% random sampling. (i) Intensity distributions along the white dashed lines in (g) and (h), comparing reconstruction quality.

shows the deviation in intensity between the 30% and 50% sampling rates and uniform sampling at the blue dashed line positions. Through a quantitative analysis of Figs. 4(a)–4(c), the MSE, SSIM, and CC for the 30% random sampling rate compared to uniform sampling are 0.0024, 0.635, and 0.6985, respectively. For the 50% random sampling rate, these values are

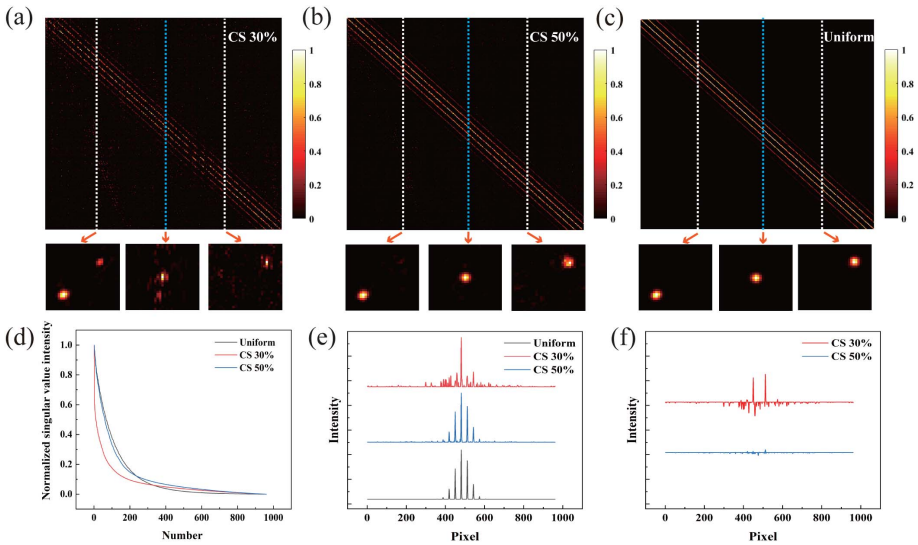

Fig. 4. RM measurement at different sampling rates. (a) RM obtained through 30% random sampling. (b) RM obtained through 50% random sampling. (c) RM obtained through uniform sampling. (d) Singular value distribution of RM at different sampling rates, highlighting that, despite some differences at lower sampling rates, the major high singular values remain consistent. (e) Intensity distributions along the blue dashed lines in (a)-(c), showing signal recovery across different sampling rates. (f) Deviations in intensity from uniform sampling at the blue dashed line positions in (a)–(c), comparing the 30% and 50% random sampling rates with uniform sampling.

0.0008, 0.8549, and 0.9153, respectively. Quantitative experimental results indicate that CS can effectively recover RM features with reduced sampling points. These results validate the effectiveness of the CS-based RM measurement method in scattering media.

To verify the imaging effectiveness of CS RM-OCT in scattering media, a housefly wing was selected as the imaging target. In the experiment, scattering was introduced by covering the surface of the housefly wing with a layer of subcutaneous chicken mucosa approximately 20 μm thick, as shown in Fig. 5(a). Figure 5(b) illustrates the intensity distribution of the light field illuminating the sample directly, where the target information is obscured by the scattered light field. The intensity distribution along the black dashed line is depicted in Fig. 5(c). To mitigate the effects of multiple scattered photons, imaging based on the RM was performed. Figures 5(d) and 5(e) present the reflection matrices obtained using 50% compressed sampling and uniform sampling, respectively. The singular value distribution, derived through the SVD of the RM, is shown in Fig. 5(f). Figures 5(g) and 5(h) display the image reconstruction results using the top 1000 singular values from the reflection matrices for compressed sampling and uniform sampling, respectively. By reconstructing the light field image from the RM, the influence of multiple scattered photons is reduced, resulting in an image contrast that is doubled compared to the light field in Fig. 5(b). Figure 5(i) shows the intensity distribution along the white dashed line, highlighting the reconstruction quality. A quantitative analysis of Figs. 5(g) and 5(h) reveals that the MSE, SSIM, and CC for the 50% random sampling rate compared to uniform sampling are 0.0074, 0.807, and 0.9063, respectively. These results indicate that even with a 50% sampling rate, the imaging target's information can be accurately recovered. This confirms the feasibility of the CS-based RM imaging method.

4. Discussion

This study presents a method that utilizes CS technology to accelerate the measurement of the RM while reducing the required number of sampling points. Traditional high sampling rates provide more information, improving reconstruction accuracy, but this also increases data acquisition time and computational burden. In contrast, lower sampling rates can reduce acquisition time and processing requirements but may lead to

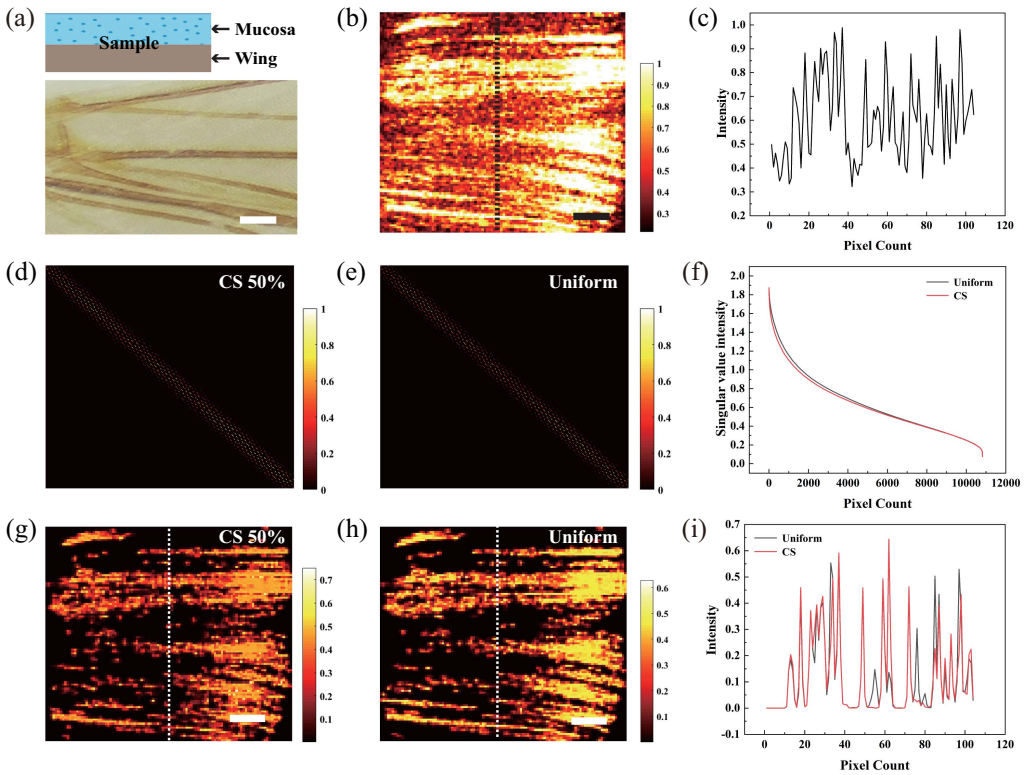

Fig. 5. RM-OCT imaging in scattering media. (a) The imaging sample, a housefly wing covered with subcutaneous chicken mucosa (approximately 20 μm thick) to introduce scattering effects. (b) The en face image of the sample, where the target information is overwhelmed by the scattered light field. (c) Intensity distribution along the black dashed line in (b), showing the effect of scattered light. (d) RM obtained using 50% compressed sampling. (e) RM obtained from uniform sampling. (f) Singular value distributions for the reflection matrices shown in (d) and (e), illustrating the impact of different sampling rates. (g) Image reconstruction using the top 1000 singular values from the RM obtained with 50% CS. (h) Image reconstruction using the top 1000 singular values from the RM obtained via uniform measurement. (i) Intensity distributions along the white dashed lines in (g) and (h), comparing image reconstruction quality between 50% CS and uniform sampling. Scale bar: 0.15 mm.

degraded image quality due to insufficient data. In our experiments, a 50% sampling rate achieved a good balance between image quality and computational efficiency, while a 30% sampling rate offered faster processing but resulted in a decline in image quality. Lower sampling rates may lead to incomplete reconstruction of the RM, as they fail to capture sufficient information to accurately restore the original light field, causing loss of image details and increased noise. To mitigate these issues, noise filtering techniques, such as Gaussian aperture filtering, can be applied during data processing to reduce the impact of noise. Additionally, during the RM reconstruction process, we can utilize prior information about the RM to constrain the procedure, thereby reducing overfitting and computational errors. Although lower sampling rates may introduce errors and decrease imaging quality, these errors can be significantly minimized through effective strategies and methods, ultimately providing reliable high-quality imaging results.

Although significant progress has been made in applying CS to RM-OCT, further exploration is needed regarding its use in complex and dynamic scenarios where rapid data acquisition is crucial for effective information retrieval. According to the scanning strategy (see Fig. 4), uniform sampling for the RM requires 961 scanning points (31×31), with each point taking approximately 80 ms to acquire, resulting in a total sampling time of about 76 s. In contrast, using a 50% sampling rate reduces the number of sampling points to approximately 480, shortening the sampling time to about 38 s. Despite the complex computational operations involved and the recovery process being proportional to the data volume, CS significantly enhances sampling efficiency. By leveraging the sparsity of the RM and applying CS techniques to reduce computational complexity, the CS program currently operates on a 2.80 GHz Intel Core i9 10900 CPU, with the recovery process taking about 100 s. The total time for RM measurement based on CS is approximately 138 s, including both data acquisition and recovery. While the overall processing time with CS is longer, it improves sampling efficiency by reducing the number of sampling points. Optimizing processing and utilizing sparsity not only reduces the required sampling points but also enhances imaging efficiency. Compared to central processing units (CPUs), GPUs offer significant advantages in matrix operations. Therefore, future work will focus on implementing GPU-based CS to further reduce processing time and enhance imaging speed, ultimately optimizing the overall imaging process.

5. Conclusion

In summary, we propose a method for measuring the RM of scattering media using CS technology to reduce measurement time. Experimental results demonstrate that the RM of scattering media is sparse, enabling effective CS sampling. This approach reduces the number of sampling points to less than half compared to traditional uniform sampling methods. CS technology provides a more efficient method for RM measurement, opening new possibilities for the application of CS-related techniques and showing potential for enhancing imaging efficiency in scattering media.

Acknowledgements

This work was supported by the Sichuan Provincial Regional Innovation Cooperation Program (No. 2023YFQ0013), the National Natural Science Foundation of China (No. 62205093), the Sichuan Science and Technology Program (Nos. 2021YFSY0063, 2021YFSY0062, 2021YFSY0064, 2021YFSY0065, 2021YFSY0066, 2022YFSY0061, 2022YFSY0062, and 2022YFSY0063), and the Hainan Province Science and Technology Special Fund (No. ZDYF2023SHFZ135).

References

1. S. Yoon, M. Kim, M. Jang, *et al.*, "Deep optical imaging within complex scattering media," Nat. Rev. Phys. **2**, 141 (2020).
2. W. Denk, J. H. Strickler, and W. W. Webb, "Two-photon laser scanning fluorescence microscopy," Science **248**, 73 (1990).
3. L. Li and L. V. Wang, "Optical coherence computed tomography," Appl. Phys. Lett. **91**, 141107 (2007).
4. J. Wang, "Data information transfer using complex optical fields: a review and perspective (Invited Paper)," Chin. Opt. Lett. **15**, 030005 (2017).
5. D. Huang, E. A. Swanson, C. P. Lin, *et al.*, "Optical coherence tomography," Science **254**, 1178 (1991).
6. J. G. Fujimoto, "Optical coherence tomography for ultrahigh resolution in vivo imaging," Nat. Biotechnol. **21**, 1361 (2003).
7. F. E. Robles, C. Wilson, G. Grant, *et al.*, "Molecular imaging true-colour spectroscopic optical coherence tomography," Nat. Photonics **5**, 744 (2011).
8. W. Wei, A. Cogliati, and C. Canavesi, "Model-based optical coherence tomography angiography enables motion-insensitive vascular imaging," Biomed. Opt. Express **12**, 2149 (2021).
9. T. R. Hillman, A. Curatolo, B. F. Kennedy, *et al.*, "Detection of multiple scattering in optical coherence tomography by speckle correlation of angle-dependent B-scans," Opt. Lett. **35**, 1998 (2010).
10. M. Adhi and J. S. Duker, "Optical coherence tomography–current and future applications," Curr. Opin. Ophthalmol. **24**, 213 (2013).
11. K. Deng, Q. Chen, Y. Bai, *et al.*, "Compact long-working-distance laser-diode-based photoacoustic microscopy with a reflective objective," Chin. Opt. Lett. **19**, 071701 (2021).
12. A. Badon, D. Li, G. Lerosey, *et al.*, "Smart optical coherence tomography for ultra-deep imaging through highly scattering media," Sci. Adv. **2**, e1600370 (2016).
13. Q. Yang, Y. Miao, T. Huo, *et al.*, "Deep imaging in highly scattering media by combining reflection matrix measurement with Bessel-like beam based optical coherence tomography," Appl. Phys. Lett. **113**, 011106 (2018).
14. S. M. Popoff, G. Lerosey, R. Carminati, *et al.*, "Measuring the transmission matrix in optics: an approach to the study and control of light propagation in disordered media," Phys. Rev. Lett. **104**, 100601 (2010).
15. A. Badon, D. Li, G. Lerosey, *et al.*, "Spatio-temporal imaging of light transport in highly scattering media under white light illumination," Optica **3**, 1160 (2016).
16. J. Cao, Q. Yang, Y. Miao, *et al.*, "Enhance the delivery of light energy ultra-deep into turbid medium by controlling multiple scattering photons to travel in open channels," Light Sci. Appl. **11**, 108 (2022).
17. J. Cao, Q. Yang, Y. Miao, *et al.*, "High-speed wavefront determination method based on single in-and-out electric field analysis to focus light through highly scattering medium," APL Photonics **6**, 036107 (2021).
18. Q. Yang, J. Cao, Y. Miao, *et al.*, "Extended imaging depth of en-face optical coherence tomography based on fast measurement of a reflection matrix by wide-field heterodyne detection," Opt. Lett. **45**, 828 (2020).
19. M. Kim, Y. Choi, C. Yoon, *et al.*, "Maximal energy transport through disordered media with the implementation of transmission eigenchannels," Nat. Photonics **6**, 581 (2012).

20. H. Lee, S. Yoon, P. Loohuis, *et al.*, "High-throughput volumetric adaptive optical imaging using compressed time-reversal matrix," Light Sci. Appl. **11**, 16 (2022).
21. M. Kim, Y. Jo, J. H. Hong, *et al.*, "Label-free neuroimaging in vivo using synchronous angular scanning microscopy with single-scattering accumulation algorithm," Nat. Commun. **10**, 3152 (2019).
22. Y. Zhang, C. Wang, S. Tong, *et al.*, "Separating single-and multiple-scattering components in laser speckle contrast imaging of tissue blood flow," Biomed. Opt. Express **13**, 2881 (2022).
23. P. Wojtaszczyk, "Stability and instance optimality for Gaussian measurements in compressed sensing," Found. Comput. Math. **10**, 1 (2010).
24. E. J. Candès, J. Romberg, and T. Tao, "Robust uncertainty principles: Exact signal reconstruction from highly incomplete frequency information," IEEE Trans. Inf. Theory **52**, 489 (2006).
25. M. Lustig, D. Donoho, and J. M. Pauly, "Sparse MRI: the application of compressed sensing for rapid MR imaging," Magn. Reson. Med. **58**, 1182 (2007).
26. Z. Guo, C. Li, L. Song, *et al.*, "Compressed sensing in photoacoustic tomography in vivo," J. Biomed. Opt. **15**, 021311 (2010).
27. N. Zhang, T. Huo, C. Wang, *et al.*, "Compressed sensing for optical coherence tomography with super-resolution imaging," Opt. Lett. **37**, 1424 (2012).
28. X. Liu and J. U. Kang, "Compressive SD-OCT: the application of compressed sensing in spectral domain optical coherence tomography," Opt. Express **18**, 22010 (2010).
29. D. Xu, N. Vaswani, Y. Huang, *et al.*, "Modified compressive sensing optical coherence tomography with noise reduction," Opt. Lett. **37**, 4209 (2012).
30. W. Liao, J. Hsieh, C. Wang, *et al.*, "Compressed sensing spectral domain optical coherence tomography with a hardware sparse-sampled camera," Opt. Lett. **44**, 2955 (2019).
31. D. Xu, Y. Huang, and J. U. Kang, "Real-time compressive sensing spectral domain optical coherence tomography," Opt. Lett. **39**, 76 (2013).
32. J. Luo, Y. Fan, H. Zhou, *et al.*, "Fabrication of different fine fiber tips for near field scanning optical microscopy by a simple chemical etching technique," Chin. Opt. Lett. **5**, S232 (2007).
33. H. Li, Z. Yu, Q. Zhao, *et al.*, "Learning-based super-resolution interpolation for sub-Nyquist sampled laser speckles," Photonics Research **11**, 631 (2023).
34. Z. Yu, H. Li, T. Zhong, *et al.*, "Wavefront shaping: a versatile tool to conquer multiple scattering in multidisciplinary fields," Innovation **3**, 100292 (2022).
35. L. Yang, T Han, J. Meng, *et al.*, "Optimized number of the primary singular values for image reconstruction in reflection matrix based optical coherence tomography," Opt. Express **30**, 2680 (2022).
36. S. Popoff, G. Lerosey, M. Fink, *et al.*, "Image transmission through an opaque material," Nat. Commun. **1**, 81 (2010).
37. Y. Yang, B. S. Kang, and Y. J. Choo, "Application of the correlation coefficient method for determination of the focal plane to digital particle holography," Appl. Opt. **47**, 817 (2008).
38. Y. Zhang, X. Li, G. Zhao, *et al.*, "Signal reconstruction of compressed sensing based on alternating direction method of multipliers," Circuits Syst. Signal Process. **39**, 307 (2020).
39. S. Chen, H. Du, L. Wu, *et al.*, "Compressed sensing MRI via fast linearized preconditioned alternating direction method of multipliers," Biomed. Eng. Online **16**, 1 (2017).
40. Z. Liu and S. Yu, "Alternating direction method of multipliers based on $\ell_{2,0}$-norm for multiple measurement vector problem," IEEE Trans. Signal Process. **71**, 3490 (2023).
41. R. Heckel and M. Soltanolkotabi, "Compressive sensing with un-trained neural networks: Gradient descent finds a smooth approximation," in *International Conference on Machine Learning* (2020), p. 4058.
42. J. Li, W. Cui, and X. Zhang, "Projected gradient descent for spectral compressed sensing via symmetric Hankel factorization," IEEE Trans. Signal Process. **72**, 1590 (2024).
43. Y. Liu, Z. Zhan, J. F. Cai, *et al.*, "Projected iterative soft-thresholding algorithm for tight frames in compressed sensing magnetic resonance imaging," IEEE Trans. Med. Imaging **35**, 2130 (2016).
44. H. Wang, S. Yang, Y. Liu, *et al.*, "Compressive sensing reconstruction for rolling bearing vibration signal based on improved iterative soft thresholding algorithm," Measurement **210**, 112528 (2023).
45. Y. Zhang, X. Li, G. Zhao, *et al.*, "Signal reconstruction of compressed sensing based on alternating direction method of multipliers," Circuits Syst. Signal Process. **39**, 307 (2020).
46. T. Van Chien, K. Q. Dinh, B. Jeon, *et al.*, "Block compressive sensing of image and video with nonlocal Lagrangian multiplier and patch-based sparse representation," Signal Process. Image Commun. **54**, 93 (2017).
47. X. Zhu, L. Lu, Z. Cao, *et al.*, "Transmission matrix-based electric field Monte Carlo study and experimental validation of the propagation characteristics of Bessel beams in turbid media," Opt. Lett. **43**, 4835 (2018).
48. P. Miao, Y. Zhang, C. Wang, *et al.*, "Random matrix description of dynamically backscattered coherent waves propagating in a wide-field-illuminated random medium," Appl. Phys. Lett. **120**, (2022).
49. Y. Wang, P. Li, C. Jiang, *et al.*, "GPU accelerated electric field Monte Carlo simulation of light propagation in turbid media using a finite-size beam model," Opt. Express **20**, 16618 (2012).
50. Q. Zhao, L. Chen, X. Hu, *et al.*, "Sub-diffraction-limit imaging with a transmission matrix in disordered media," Opt. Lett. **41**, 2118 (2016).
51. J. Dai, Y. Xu, F. Zhang, *et al.*, "Novel imaging method based on spatially varying transmission matrices for enhanced resolution in complex scattering media," Biomed. Opt. Express **12**, 4130 (2021).
52. L. Zhang, Y. Huang, X. Li, *et al.*, "High-resolution optical imaging through scattering media with a dual-polarization approach," Sci. Rep. **12**, 8914 (2022).